ADVANCED ENERGY MATERIALS

Supporting Information

for *Adv. Energy Mater.,* DOI: 10.1002/aenm.201902509

Suppressed Deep Traps and Bandgap Fluctuations in Cu_2CdSnS_4 Solar Cells with ~8% Efficiency

*Shreyash Hadke, Sergiu Levcenko, Gopalakrishnan Sai Gautam, Charles J. Hages, José A. Márquez, Victor Izquierdo-Roca, Emily A. Carter, Thomas Unold, and Lydia H. Wong**

Supporting Information

Suppressed deep traps and band-gap fluctuations in Cu_2CdSnS_4 solar cells with ~8% efficiency

*Shreyash Hadke, Sergiu Levcenko, Gopalakrishnan Sai Gautam, Charles J Hages, José A. Márquez, Victor Izquierdo-Roca, Emily A. Carter, Thomas Unold, Lydia H. Wong**

1) Figure S1 shows the structures used for simulating XRD patterns. All the patterns are simulated using the software VESTA (http://jp-minerals.org/vesta/en/).[52] The optimized lattice parameters, from our DFT-SCAN calculations, are a,b = 0.54 nm and c = 1.08 nm for kesterite Cu_2ZnSnS_4 and a,b = 0.56 nm and c = 1.09 nm for stannite Cu_2CdSnS_4; these parameters are used for XRD simulations.

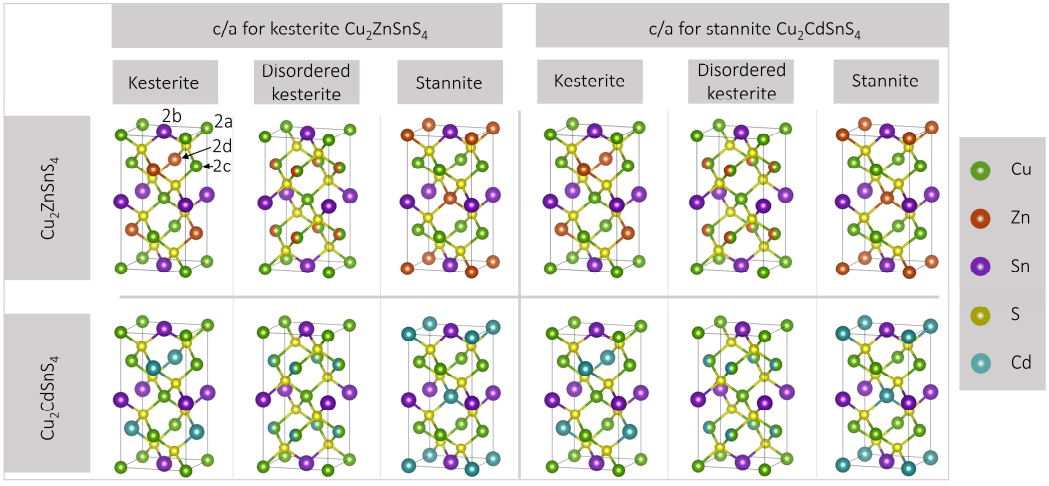

Figure S1: Structures used for simulating XRD patterns

2) Reasons for using the narrow 2Θ range of 15 to 24 degrees for studying the differences in the kesterite and stannite structures:

Figure S2 shows the simulated XRD patterns for Cu_2CdSnS_4 under six difference conditions. Comparing the XRD patterns, we observe that there are five distinct changes in different 2Θ ranges.

a. Between the 2Θ range of 15 to 25 degrees, there is a single intense peak at 18.2 degrees for the kesterite Cu_2CdSnS_4 (having c/a for kesterite Cu_2ZnSnS_4) while there are two intense peaks at 16.4 and 22.5 degrees for stannite Cu_2CdSnS_4 (having c/a for stannite Cu_2CdSnS_4). Moreover, the single intense peak at 18.2 degrees does not vary even when the c/a ratio is changed in the kesterite structure. Similar observations are evident when comparing stannite and disordered kesterite structure. Hence, the peaks in this range can be used reliably to determine the structure of Cu_2CdSnS_4. Note the three peaks at ~16, 18, and 22 degrees are present in both structures and here we compare the relative intensities.
b. The main peak corresponding to 112 reflections shifts from 28.4 to 27.9 degrees. But this change is subtle and also depends on the c/a ratio used.
c. Comparing the peaks in the 2Θ range of 32 to 33 degrees for kesterite Cu_2CdSnS_4 (having c/a for kesterite Cu_2ZnSnS_4) and stannite Cu_2CdSnS_4 (having c/a for stannite Cu_2CdSnS_4), we observe a splitting of peaks. However, this splitting is also affected by the changes in c/a ratio, as seen in the XRD pattern for kesterite Cu_2CdSnS_4 (having c/a for stannite Cu_2CdSnS_4), and hence, these peaks cannot be used to determine the structure of Cu_2CdSnS_4. Similar results are observed if the disordered kesterite structure is considered instead of the kesterite structure.
d. The peaks in the range 45 to 47 degrees follow a similar trend as described in (c).

e. The peaks in the range 54 to 56 degrees follow a similar trend as described in (c).

Hence, the only peaks that can be used to determine the structure of Cu_2CdSnS_4 between stannite and kesterite are the peaks in the range 15 to 24 degrees; therefore this range is used in the discussion in the main text. Note that the simulations correspond to 'powder XRD', that is, no preferential orientation effects, while the experimental data is for thin-film samples, where the effects of texture cannot be discarded. Hence, although we use the intensity ratio between different peaks to assign the crystal structure, these ratios might be affected to some degree by texture effects.

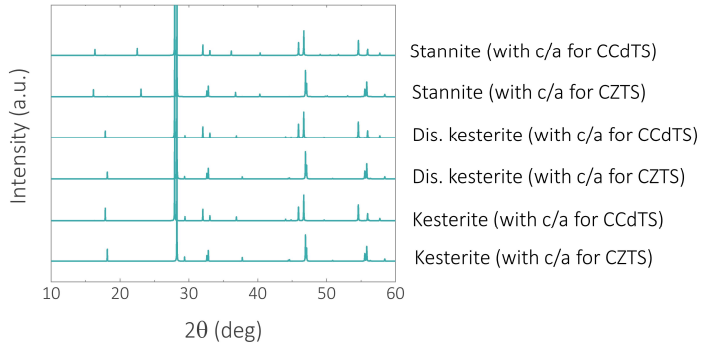

Figure S2: Simulated XRD patterns for different Cu_2CdSnS_4 structures

3)

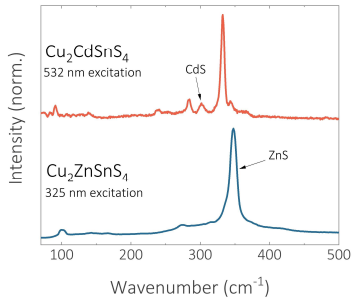

Figure S3: Raman spectra of Cu_2CdSnS_4 and Cu_2ZnSnS_4 under the resonant excitation conditions for CdS (532 nm) and ZnS (325 nm).

4)

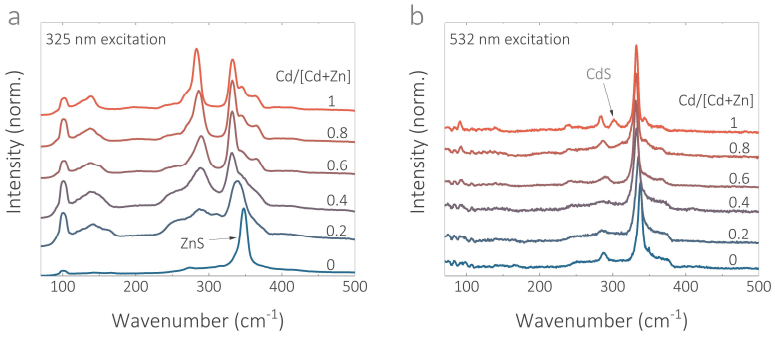

Figure S4: Raman spectra of $Cu_2(Zn,Cd)SnS_4$ under the resonant excitation conditions for CdS (532 nm) and ZnS (325 nm).

5)

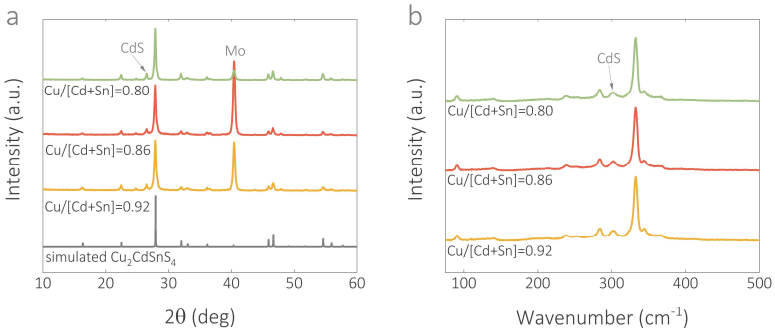

Figure S5: XRD patterns and Raman spectra (532 nm excitation) for Cu_2CdSnS_4 having Cu/[Cd+Sn] ratio of 0.8, 0.86, and 0.92.

6)

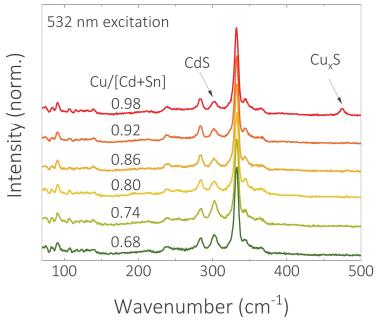

Figure S6: Raman spectra for Cu_2CdSnS_4 having Cu/[Cd+Sn] ratio of 0.68, 0.74, 0.80, 0.86, 0.92, and 0.98.

7) Based on the constraints used for simulations, we predict that the experimental conditions correspond to the chemical potential region bounded by 'Cu-poor' and 'constrained Cu-poor'. This is because

a) Cu-rich simulations have metallic copper in equilibrium. This is not observed experimentally, either in the precursor solution, or in the sulphurized film.

b) Experimentally, in the precursor solution and in the sulphurized film, we have a Cu-poor, Sn-poor, and Zn-rich composition.

c) The end points in the highlighted region in gray correspond to the most negative copper chemical potential where CZTS is stable under Zn- and Sn-rich chemical potentials, and the most negative Cu chemical potential without any constraints for Zn and Sn (basically, both Zn and Sn can be poor here).

Hence, for our case of Cu-poor, Zn-rich, and Sn-poor composition, the area in the gray region should correspond to the experimental composition.

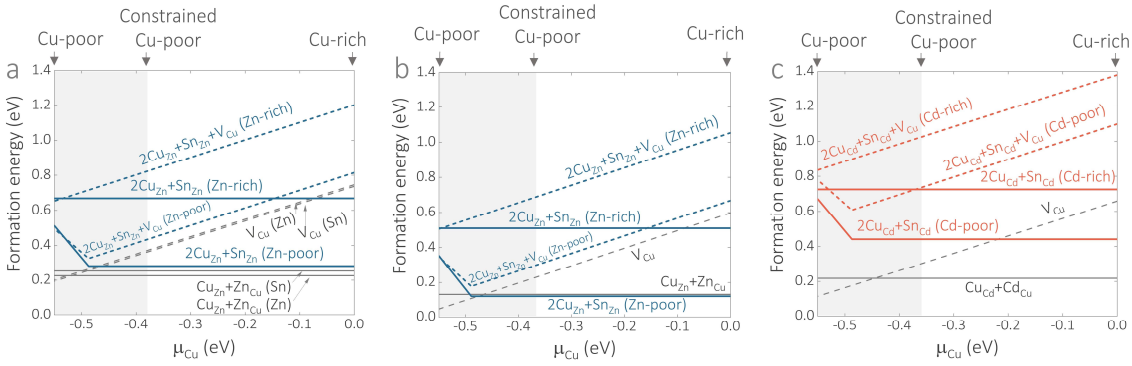

Figure S7: DFT-SCAN defect formation energies for (a) kesterite Cu_2ZnSnS_4, (b) stannite Cu_2ZnSnS_4, and (c) stannite Cu_2CdSnS_4.

8)

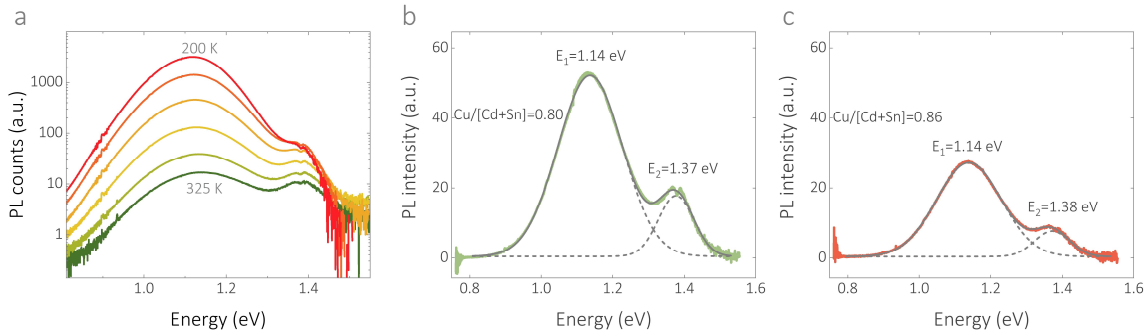

Figure S8: (a) Temperature-dependent PL for a Cu_2CdSnS_4 device with Cu/[Cd+Sn]=0.80, showing the change in the relative intensity of the defect and band-to-band peak; (b) fitting of the room-temperature PL spectra on a Cu_2CdSnS_4 device with Cu/[Cd+Sn]=0.80; (c) fitting of the room-temperature PL spectra on a Cu_2CdSnS_4 device with Cu/[Cd+Sn]=0.86. There is a small difference in the band gap extracted from the EQE data and from the PL data. We attribute this difference to the fact that the two PL bands overlap such that the Gaussian fit for the PL shape might not be valid in the low-energy part of the band-to-band transition, and to the differences associated with bandgap measurements using optical (PL and UV-vis) and electrical (EQE) methods.

9)

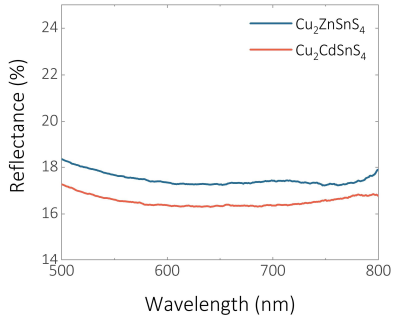

Figure S9: Reflectance data for Cu_2ZnSnS_4 and Cu_2CdSnS_4 measured on Glass/Mo/Absorber using an integrating sphere UV-vis setup

10)

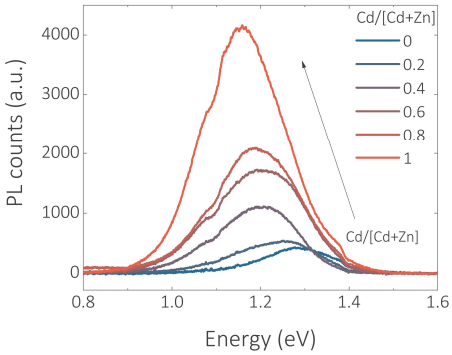

Figure S10: Room temperature steady-state PL of $Cu_2(Zn,Cd)SnS_4$ thin films.

11)

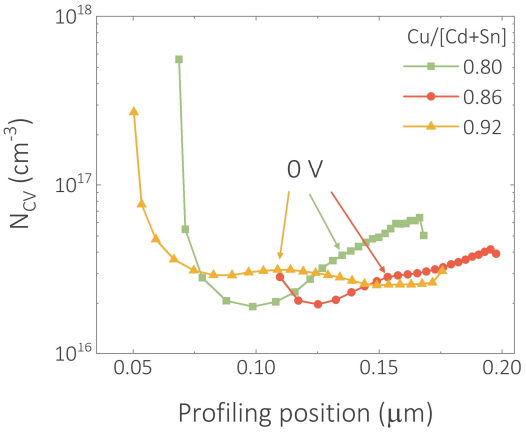

Figure S11: Calculated charge-carrier density from capacitance-voltage measurements for Cu_2CdSnS_4 with different Cu/[Cd+Sn] ratios.

The profiles show a typical U-shape often observed for chalcogenide thin film semiconductors.[37] The charge-carrier density can be estimated from the modest bias voltage conditions (around 0 V bias) where the profile is relatively flat or exhibits a minimum. The data points toward small profiling position are obtained from relatively large forward bias (0.6 V) and do not reflect realistic carrier densities but are rather shown for completeness.

12)

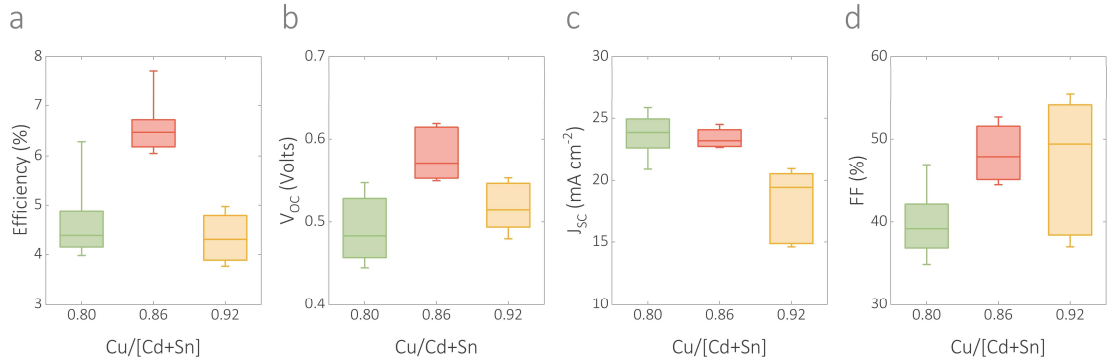

Figure S12: Statistical data for 10 Cu_2CdSnS_4 devices at each composition.

13)

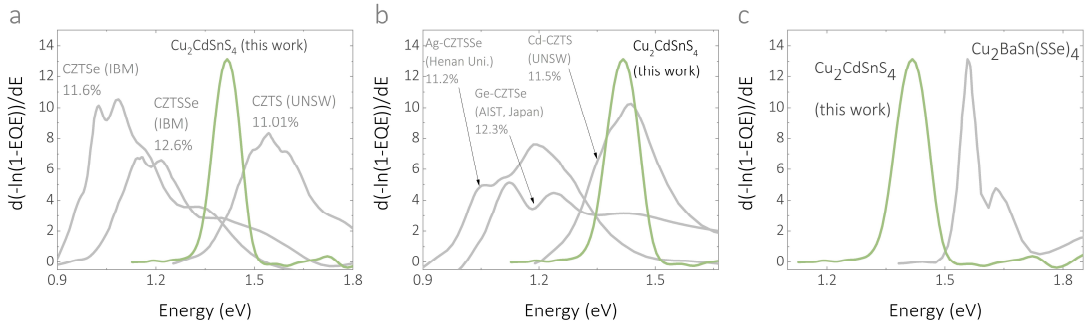

Figure S13: Band-gap fluctuations as characterized by data extracted from EQE measurements for different high-efficiency devices[3, 7, 9, 42, 43, 44] published in the literature. Band-gap fluctuations are proportional to the FWHM of the peaks.

14)

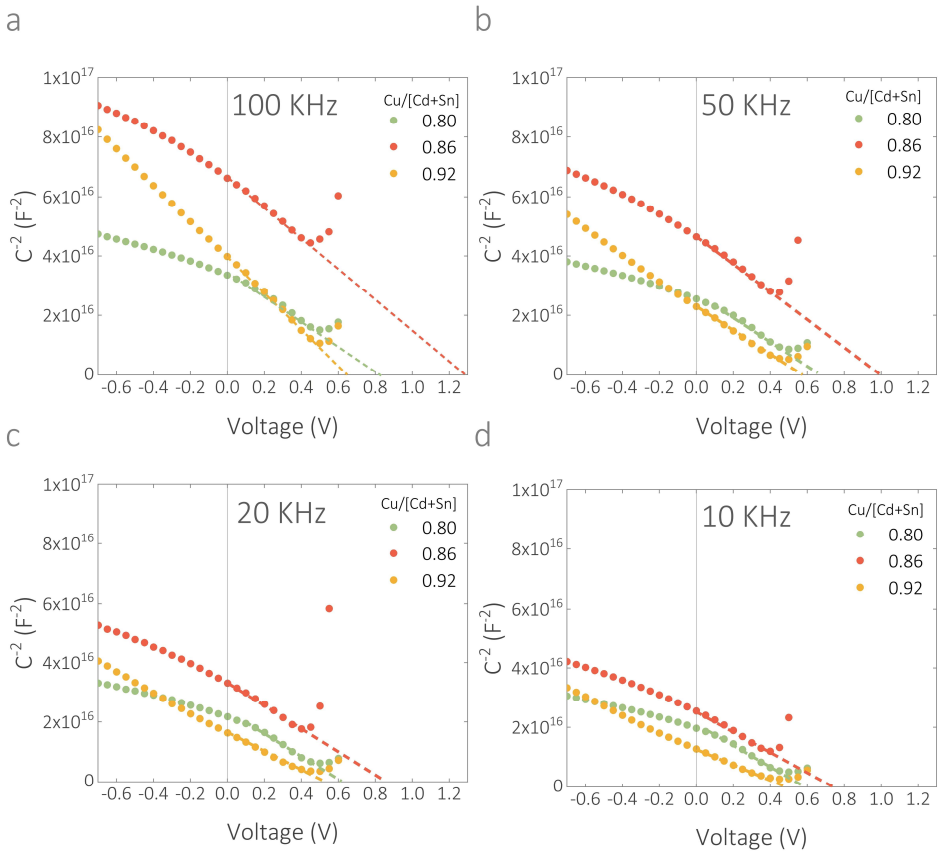

Figure S14: Capacitance-voltage measurements for Cu_2CdSnS_4 at different AC perturbation frequencies.